Physica D 414 (2020) 132695

Contents lists available at ScienceDirect

Physica D

journal homepage: www.elsevier.com/locate/physd

Resolving soil and surface water flux as drivers of pattern formation in Turing models of dryland vegetation: A unified approach

Eric Siero *

Institute for Mathematics, Carl von Ossietzky University of Oldenburg, 26111 Oldenburg, Germany
Department of Earth Sciences, Utrecht University, 3584 CB Utrecht, The Netherlands

ARTICLE INFO

Article history:
Received 13 October 2019
Received in revised form 12 August 2020
Accepted 14 August 2020
Available online 21 August 2020
Communicated by E. Gilad

Keywords:
Reaction–diffusion
Desertification
Self-organization
Model comparison
Model reduction
Minimal model

ABSTRACT

Over the past two decades, multi-component dryland vegetation models have been successful in qualitatively reproducing the spatial vegetation patterns widely observed in nature. In the two-component (water, vegetation) Klausmeier model, water flow from bare to vegetated areas drives pattern formation. The more elaborate Rietkerk and Gilad three-component models make a distinction between soil and surface water. In this article the three models are approximated from within a unifying framework, with a focus on processes that drive pattern formation, in order to promote the understanding of similarities and differences between these models. Reduction from a model with a separate soil and surface water component, to a model with a single water component, preserves Turing instability in all but one of the cases studied.

1. Introduction

Since the 1950s it has been known that vegetation forms large-scale spatial patterns in drylands [1]. Analysis of satellite data has established that they are ubiquitous in drylands around the world [2]. Apart from being an intriguing phenomenon, it has been proposed that these patterns can act as a spatial early warning signal for an upcoming transition to bare desert [3–5]. As such, ultimately, they could be used to help mitigate the consequences of climate change.

In absence of spatial heterogeneity, dryland vegetation patterns are a consequence of self-organization [6]. Vegetation presence enhances the water infiltration capacity [7], resulting in overland water flow (run-on) toward areas with vegetation [8], increasing soil moisture in vegetated patches [9]. Thus, the persistence of vegetated patches with patches of bare soil may be explained by a positive plant–soil feedback [9], that initiates a scale-dependent feedback mechanism [10]. The mechanism of increased infiltration in vegetated patches is present in the Rietkerk and Gilad model [11,12], and implicitly in the Klausmeier model [6]. The local facilitation (through increased water infiltration), combined with long range competition for water, has been identified as a driver of pattern formation through Turing instability [10].

A Turing instability [13] occurs when a spatially homogeneous steady state in a spatially homogeneous model becomes unstable against a perturbation with a finite wavelength. The simplest reaction–diffusion models exhibiting Turing patterns are two-component activator–inhibitor models with fast inhibitor diffusion (relative to diffusion of the activator), as in the Klausmeier model [6] with water advection replaced by diffusion [14]. In models with three or more components (e.g. the Rietkerk and Gilad model), a Turing instability need not be stationary [13]: the emerging Turing pattern may be a wave train (in arbitrary direction). In this article this wave instability is referred to as a Turing–Hopf instability. In reaction–diffusion models with advection (through downhill flow of water), emerging Turing patterns generally move uphill [15,16]; in this article the soil surface is always modeled to be flat.

A necessary condition for Turing instability in two-component dryland models is self-activation of the vegetation: in response to a small increase in vegetation, vegetation (initially) grows further. In the Klausmeier model the increased infiltration at locations with vegetation is represented by self-activation. In the Gilad model, self-activation is the result of a root-to-shoot ratio that increases with standing biomass, so that a flux of water toward vegetated areas can arise due to differences in the uptake rate [17]. In three-component models, self-activation is not a necessary condition for Turing pattern formation, as exemplified by the Rietkerk model.

In summary, the presence of vegetation can both increase the infiltration rate and the per capita uptake rate (by a varying root-to-shoot ratio), and both can create a flux of (above respectively

* Correspondence to: Department of Earth Sciences, Utrecht University, 3584 CB Utrecht, The Netherlands.
E-mail address: e.p.j.a.siero@uu.nl.

https://doi.org/10.1016/j.physd.2020.132695

below ground) water toward vegetation, thereby enabling Turing pattern formation. Three different models implement one (Klausmeier, Rietkerk) or both (Gilad) of these pattern forming mechanisms and all qualitatively reproduce observed patterns [18]. In the Klausmeier model, where in this article the water component is interpreted as surface water, water consumption is a combined process of infiltration and uptake, compromising opportunities to validate the model with field measurements. The Rietkerk and Gilad models do make a distinction between soil and surface water, but the extra model component makes analysis more involved.

In this article, the three models and their pattern forming mechanisms are approximated from within a single three-component unification model framework, to identify fundamental similarities and differences between models. A detailed Turing analysis reveals necessary conditions on the functional form of the infiltration and uptake functions. Reductions to simpler two-component models are performed, showing that Turing instability is preserved, except if vegetation is not self-activating and surface water flux is neglected. Bifurcating Turing patterns are numerically continued, opening up pathways toward model comparison in the nonlinear regime. These techniques can be used to make an informed modeling decision dependent on field measurement and remote sensing data availability.

2. Methods: unification, reduction, Turing analysis and numerical continuation

2.1. Existing framework and reductions

A fairly general three-component (surface water density H, soil water density W, vegetation density B) dryland reaction–diffusion model is given by:

$$\begin{cases} H_t &= d_1\Delta H &-l_1 H &+p &-r_2 H\cdot I(B) & \\ W_t &= d_2\Delta W &-l_2 W & &+r_2 H\cdot I(B) &-r_1 U(W,B) \\ B_t &= d_3\Delta B &-l_3 B & & &+jr_1 U(W,B). \end{cases} \tag{1}$$

The Laplace operator $\Delta = \partial_x^2 + \partial_y^2$ is used to model spread of water and vegetation. Each component diffuses with diffusion constants d_1, d_2 and $d_3 > 0$ and experiences a linear loss with rate l_i due to evaporation, seepage or mortality. The rainfall parameter p represents average rainfall on the climatic time scale, which varies slowly; in this article it is taken to be independent of time. The infiltration is a linear function of H. The parameter j measures the gain in vegetation B per converted unit of soil water W.

We assume a flat soil surface, so without downhill flow of surface water through advection, which would have its own influence on pattern formation [15]. The framework (1) encompasses the Rietkerk model [11,19] and also the simplified Gilad model [20,21], except that in the Gilad model surface water diffusion is nonlinear and l_2 and j are not constant. The Klausmeier model [6] is similar to (1), but it only has one water component and its water advection would need to be replaced by diffusion [14].

We now view two special cases of (1), referred to here as 'sandy-soil' and 'sticky-soil', that can also be studied as reduced two-component systems.

2.1.1. Sandy-soil: without surface water flux

If surface water infiltration is a fast process (e.g. for sandy soil [20]), it results in low surface water density. Accordingly, we write $r_2 = \tilde{r}_2/\epsilon$ and $H = \epsilon\tilde{H}$ and substituting this is into the first equation of (1) yields

$$\epsilon\tilde{H}_t = \epsilon d_1\Delta\tilde{H} - \epsilon l_1\tilde{H} + p - \tilde{r}_2\tilde{H}\cdot I(B)$$

which after $\epsilon \to 0$ and substitution back leads to the algebraic equation $r_2 H\cdot I(B) = p$; then (1) reduces to:

$$\begin{cases} W_t &= d_2\Delta W &-l_2 W &+p &-r_1 U(W,B) \\ B_t &= d_3\Delta B &-l_3 B & &+jr_1 U(W,B). \end{cases} \tag{2}$$

If infiltration is only a fast process compared to other surface water processes, but not compared to soil water and biomass processes, then:

$$\begin{cases} H_t &= & &+p &-r_2 H\cdot I(B) & \\ W_t &= d_2\Delta W &-l_2 W & &+r_2 H\cdot I(B) &-r_1 U(W,B) \\ B_t &= d_3\Delta B &-l_3 B & & &+jr_1 U(W,B) \end{cases} \tag{3}$$

which has the same steady states (and stationary bifurcations) as (2) (but different dynamics). Stability of a steady state of (3) implies stability of the corresponding steady state of (2), but Hopf-instability will not always be preserved.

2.1.2. Sticky-soil: without soil water flux

If soil water diffusion is a slow process, in the limit this can be modeled by $d_2 = 0$, a situation referred to here as 'sticky-soil'. For reasons of economy it can be worth to carry out a subsequent reduction. By computing W_{st} solving

$$0 = -l_2 W + r_2 H\cdot I(B) - r_1 U(W,B),$$

followed by insertion in the reduced model

$$\begin{cases} H_t &= d_1\Delta H &-l_1 H &+p &-r_2 H\cdot I(B) \\ B_t &= d_3\Delta B &-l_3 B & &+jr_1 U(W_{\mathrm{st}},B) \end{cases} \tag{4}$$

which has equal steady states (and stationary bifurcations) as (1) with $d_2 = 0$. Again, stability of a steady state of (1) with $d_2 = 0$ implies stability of the corresponding steady state of (4), but Hopf-instability is not generally preserved. One could also arrive at (4) by assuming $r_1 = \tilde{r}_1/\epsilon$, $l_2 = \tilde{l}_2/\epsilon$, $W = \epsilon\tilde{W}$, $U(W,B) = W\cdot\tilde{U}(B)$ and $\epsilon \to 0$ as in Section 2.1.1.

2.2. Unification model

The 'unification model' is a multi-linear Rietkerk model with surface water evaporation, with an uptake term that is optionally nonlinearly dependent on biomass, in which case it is a further simplification of the Gilad model. It is defined by (1) with

$$\begin{cases} I(B) &= B \\ U(W,B) &= WB(1+\eta B)^q \end{cases} \tag{5}$$

so in full it reads:

$$\begin{cases} H_t &= d_1\Delta H &-l_1 H &+p &-r_2 HB & \\ W_t &= d_2\Delta W &-l_2 W & &+r_2 HB &-r_1 WB(1+\eta B)^q \\ B_t &= d_3\Delta B &-l_3 B & & &+jr_1 WB(1+\eta B)^q. \end{cases} \tag{6}$$

The unification model with $\eta = 0$ mimics the Rietkerk model (Section 4) and with $\eta > 0$ mimics the simplified Gilad model (Section 5). It has twelve parameters with five relationships: space, time, H, W and B can be scaled. To keep the connection with real-world quantities as clear as possible, no scaling is performed. Choosing precipitation p as a free parameter, this means that 11 parameter values need to be chosen. Because measurement of parameters is scarce and possibly site-specific, parameter values in the literature can be based on rough estimations. In Table 1 the implied parameters for the unification model, based on parameter values from previous articles, show significant variation.

Quantitative comparison of model output with real ecosystems requires reliable estimation of the parameters. A common practice is to choose parameters in such a way that the outcome at least has realistic dimensions. With so many parameters to choose, this problem is underdetermined and the approach would

be highly subjective. Instead, in this article, the default parameter value is taken to be equal to 1, and deviations from this are explained below. The consequence is that results are qualitative, which is why the mention of units in figures below will be suppressed. The advantage is that it becomes more transparent which parameter choices are crucial to observe qualitative dynamics.

There are clear differences in the values of the diffusion coefficients d_1, d_2 and d_3 in Table 1, generally $d_1 \gg d_2 \gg d_3$. For the unification model we choose $d_1 = 10000$, $d_2 = 100$ and $d_3 = 1$, meaning that surface water spreads 10 times faster than soil water and 100 times faster than vegetation. Alternative values are $d_2 = 0$ (without soil water flux, Section 2.1.2) and $d_1 = 0$ (without surface water flux), a more proper way to achieve this is by letting $r_2 \to \infty$ (Section 2.1.1).

Comparisons are made between surface water evaporation rate $l_1 = 0$ and $l_1 = 1$ to study the effect of its presence, as it is absent in the original Rietkerk and Gilad models [11,12]. Vegetation is typically measured as dry mass, so that $j < 1$ reflects that plants consist for a large portion out of water. The parameter j is taken to be smaller than the portion of dry mass, to take into account the use of water in (and subefficiency of) the photosynthesis process.

Parameter $\eta > 0$ represents vegetation that is more effective at taking up water, through an increasing per capita rate (autocatalysis). In the Gilad model this disproportionate uptake is through an extended root system and η is related to the root-to-shoot ratio. In the unification model either $\eta = 0$ or $\eta = 1$; note that negative η would result in logistic growth. The power parameter q determines how nonlinear this effect is. Although $q = 2$ in the simplified Gilad model, in the unification model $q = 1$ to have the lowest order correction to the model with $\eta = 0$.

2.3. Notation and Turing analysis

For use in the analysis of the dryland models, we introduce some notation and useful observations on Turing instability in three-component reaction–diffusion systems; background and details for both two- and three-component systems are given in Appendix A. A general three-component reaction–diffusion system (without cross-diffusion) is given by:

$$\begin{cases} u_t &= d_1 \Delta u + f(u,v,w) \\ v_t &= d_2 \Delta v + g(u,v,w) \\ w_t &= d_3 \Delta w + h(u,v,w). \end{cases}$$

The Jacobian of the reaction terms is given by

$$A := \begin{pmatrix} a_{11} & a_{12} & a_{13} \\ a_{21} & a_{22} & a_{23} \\ a_{31} & a_{32} & a_{33} \end{pmatrix} := \begin{pmatrix} \frac{\partial f}{\partial u} & \frac{\partial f}{\partial v} & \frac{\partial f}{\partial w} \\ \frac{\partial g}{\partial u} & \frac{\partial g}{\partial v} & \frac{\partial g}{\partial w} \\ \frac{\partial h}{\partial u} & \frac{\partial h}{\partial v} & \frac{\partial h}{\partial w} \end{pmatrix}$$

which in case of the unification model (6) is:

$$A = \begin{pmatrix} -l_1 - r_2 B & 0 & -r_2 H \\ r_2 B & -l_2 - r_1 B(1+\eta B)^q & r_2 H - r_1 W\left((1+\eta B)^q + q\eta B(1+\eta B)^{q-1}\right) \\ 0 & j r_1 B(1+\eta B)^q & -l_3 + j r_1 W\left((1+\eta B)^q + q\eta B(1+\eta B)^{q-1}\right) \end{pmatrix}. \tag{7}$$

The first principal minors are denoted by

$$\begin{aligned} A_{1,1} &= a_{22}a_{33} - a_{23}a_{32}, \\ A_{2,2} &= a_{11}a_{33} - a_{13}a_{31}, \\ A_{3,3} &= a_{11}a_{22} - a_{12}a_{21}, \end{aligned}$$

where the subindices of A indicate which row and column are excluded before the determinant is taken.

The spectrum of a steady state $(\bar{u}, \bar{v}, \bar{w})$ is given by the solutions $\lambda(k)$ of the dispersion relation $\det(M - \lambda I) = 0$, where $M = A(\bar{u}, \bar{v}, \bar{w}) - Dk^2$ and $D = \mathrm{diag}(d_1, d_2, d_3)$ is the diagonal matrix with entries d_1, d_2, d_3. So

$$\det(M - \lambda I) = -\lambda^3 + \beta_2(k)\lambda^2 + \beta_1(k)\lambda + \beta_0(k) = 0 \tag{8}$$

where

$$\begin{aligned} \beta_0(k) &= \det(M) \\ \beta_1(k) &= -M_{1,1} - M_{2,2} - M_{3,3} \\ \beta_2(k) &= \mathrm{tr}(M) = \mathrm{tr}(A) - (d_1 + d_2 + d_3)k^2 < 0 \end{aligned}$$

where $M_{i,i}$ are again the first principal minors. From the Routh–Hurwitz criterion (Appendix A.2), the functions

$$\begin{aligned} \beta_0(k) = -d_1 d_2 d_3 k^6 + (d_1 d_2 a_{33} + d_1 d_3 a_{22} + d_2 d_3 a_{11}) \\ \times\ k^4 - (d_1 A_{1,1} + d_2 A_{2,2} + d_3 A_{3,3})k^2 + \det(A) \end{aligned} \tag{9}$$

$$\beta_0(k) + \beta_1(k)\beta_2(k) = \gamma_6 k^6 + \gamma_4 k^4 + \gamma_2 k^2 + \gamma_0 \tag{10}$$

where

$$\begin{aligned} \gamma_0 &= \det(A) - \mathrm{tr}(A)(A_{1,1} + A_{2,2} + A_{3,3}), \\ \gamma_2 &= \mathrm{tr}(A)(d_1(a_{22} + a_{33}) + d_2(a_{11} + a_{33}) + d_3(a_{11} + a_{22})) \\ &\quad + (d_1 + d_2 + d_3)(A_{1,1} + A_{2,2} + A_{3,3}) - (d_1 A_{1,1} + d_2 A_{2,2} + d_3 A_{3,3}), \\ \gamma_4 &= d_1 d_2 a_{33} + d_1 d_3 a_{22} + d_2 d_3 a_{11} - \mathrm{tr}(A)(d_1 d_2 + d_1 d_3 + d_2 d_3) \\ &\quad - (d_1 + d_2 + d_3)(d_1(a_{22} + a_{33}) + d_2(a_{11} + a_{33}) + d_3(a_{11} + a_{22})), \\ \gamma_6 &= (d_1 + d_2 + d_3)(d_1 d_2 + d_1 d_3 + d_2 d_3) - d_1 d_2 d_3 > 0. \end{aligned}$$

are relevant for linear stability, as defined below here. Let $(\bar{u}, \bar{v}, \bar{w})$ denote a spatially homogeneous steady state.

Definition. If, for given $k > 0$, $\beta_0(k) > 0$, then $(\bar{u}, \bar{v}, \bar{w})$ is *Turing unstable against wavenumber k*. If $(\bar{u}, \bar{v}, \bar{w})$ is stable against spatially homogeneous perturbations and, for some $k > 0$, Turing unstable against wavenumber k, then $(\bar{u}, \bar{v}, \bar{w})$ is *Turing unstable*.

If, for given $k > 0$, $\beta_0(k) + \beta_1(k)\beta_2(k) < 0$ while $\beta_0(k), \beta_1(k) < 0$, then $(\bar{u}, \bar{v}, \bar{w})$ is *Turing–Hopf unstable against wavenumber k*. If $(\bar{u}, \bar{v}, \bar{w})$ is stable against spatially homogeneous perturbations and, for some $k > 0$, Turing–Hopf unstable against wavenumber k, then $(\bar{u}, \bar{v}, \bar{w})$ is *Turing–Hopf unstable*.

Note that, from these definitions, any spatially homogeneous steady state that is not stable against spatially homogeneous perturbations is automatically not Turing(-Hopf) unstable.

Lemma 1 (*No Turing Instability*). *If $a_{11}, a_{22}, a_{33} \le 0$ and $A_{1,1}, A_{2,2}, A_{3,3} \ge 0$, then $(\bar{u}, \bar{v}, \bar{w})$ is not Turing unstable.*

Proof. Suppose that $(\bar{u}, \bar{v}, \bar{w})$ is stable against spatially homogeneous perturbations, then $\det(A) < 0$. Thus, using the assumptions on a_{ii} and A_{ii}, all terms of $\beta_0(k)$ are negative (or zero). □

Lemma 2 (*No Turing–Hopf Instability*). *If $a_{11}, a_{22}, a_{33} \le 0$ and $A_{2,2}, A_{3,3} \ge 0$, then $(\bar{u}, \bar{v}, \bar{w})$ is not Turing–Hopf unstable if $A_{1,1} \ge 0$ or $d_1 \ge d_2, d_3$.*

Proof. Suppose that $(\bar{u}, \bar{v}, \bar{w})$ is stable against spatially homogeneous perturbations, then $\gamma_0 > 0$, in particular $A_{1,1} + A_{2,2} + A_{3,3} > 0$. From $a_{11}, a_{22}, a_{33} \le 0$ it follows that $\gamma_4 > 0$. If $A_{1,1} \ge 0$ or $d_1 \ge d_2, d_3$ it follows that also $\gamma_2 > 0$. □

Lemma 3 (*Mutual Exclusivity of Turing and Turing–Hopf Instability*). *For given k, $(\bar{u}, \bar{v}, \bar{w})$ cannot be both Turing unstable and Turing–Hopf unstable against wavenumber k.*

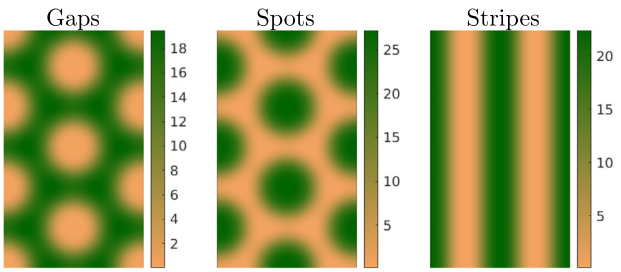

Fig. 1. Vegetation component of pattern steady states with critical wavenumber that fit the domain Ω.

Proof. By definition, wavenumber k Turing unstable implies $\beta_0(k) > 0$, whereas wavenumber k Turing–Hopf unstable implies $\beta_0(k) < 0$. □

2.4. Setup of continuation of spatial patterns in two space dimensions

To compute steady states and their stability, the software package *pde2path* [22] (with the routine *pmcont* to avoid 'branch jumping' [23]) is used. Let k_c be the length of the (Turing-)critical wavevectors. Since the models in this paper are isotropic, with a slight abuse of language, the length of the wavevector will be referred to as the wavenumber. A rectangular computational domain Ω is chosen:

$$\Omega = \left[-\frac{2\pi}{k_c}, \frac{2\pi}{k_c}\right] \times \left[-\sqrt{3}\frac{2\pi}{k_c}, \sqrt{3}\frac{2\pi}{k_c}\right]$$

with periodic boundary conditions in the first dimension and Neumann boundary conditions in the second. This domain exactly fits both the critical 2-stripe pattern and the hexagonal patterns with 6 gaps/spots, see Fig. 1. Only these patterns are computed, e.g. patterns with a different wavenumber are beyond the scope of this article. Also, (spectral) stability is against perturbations on Ω and excludes stability against e.g. large wavelength perturbations.

Because the computation of patterns is restricted to critical wavenumber patterns, the possibility of transitions to patterns with lower wavenumbers is not captured. Like the transition from gaps to stripes to spots [25], transitions to smaller wavenumbers are typically observed in model studies with (slowly) decreasing precipitation [14,15,26]. At low precipitation, the last stable pattern could thus be a single spot of vegetation in an otherwise bare desert, but other scenarios (e.g. in the presence of sustained grazing [27,28]) are also possible.

3. The Klausmeier model

More than two decades ago, the first multi-component model was introduced that accounted for water redistribution toward vegetated areas as a driver of vegetation pattern formation: water flows down a hill slope until it reaches vegetation and is absorbed. In the present article, flow downhill (modeled by advection) is replaced by diffusion, which is customary on flat terrain [14]. This version of the model is almost identical to the Gray–Scott model [29–31], but in the context of this article it will be referred to as the (flat) Klausmeier model. The flat Klausmeier model has two components (water density H, vegetation density B) and is given by:

$$\begin{cases} H_t &= d_1\Delta H &-l_1 H &+p &-C(H,B) \\ B_t &= d_3\Delta B &-l_3 B & &+jC(H,B). \end{cases} \tag{11}$$

Without the explicit distinction between soil and surface water, the function C is a composition of infiltration and uptake. In the Klausmeier model, it is expressed as a product,

$$C(H,B) = rG(H)F(B)B = rHB^2, \tag{12}$$

where $G(H) = H$ models the functional response of plants to water and $F(B) = B$ models the amelioration of soil infiltration characteristics by vegetation [6]. The modeling of C by a product of F and G is not further substantiated in [6], but yields a conceptual representation of the notion of local facilitation.

The positive spatially homogeneous steady states of (11) are, for $p \geq \frac{2l_3}{j}\sqrt{\frac{l_1}{r}}$,

$$B_\pm = \frac{jp}{2l_3} \pm \sqrt{\left(\frac{jp}{2l_3}\right)^2 - \frac{l_1}{r}} \quad \text{with} \quad H_\pm = \frac{l_3}{j}\frac{1}{rB_\pm},$$

where only (H_+, B_+) is possibly stable against spatially homogeneous perturbations. The Jacobian of the reaction terms is

$$A = \begin{pmatrix} -l_1 - rB^2 & -2rHB \\ jrB^2 & -l_3 + 2jrHB \end{pmatrix}$$

and evaluated in (H_+, B_+):

$$A_+ = \begin{pmatrix} -l_1 - rB_+^2 & -\frac{2l_3}{j} \\ jrB_+^2 & l_3 \end{pmatrix}.$$

Naturally $l_3 > 0$, so B is self-activating which is a necessary condition for Turing instability (Appendix A.1), and the system corresponds to the left panel of Fig. A.8. Choosing $P = p/l_1$ and replacing H by $P - H$, *lack of water* is an inhibitor [32], as in the right panel of Fig. A.8.

3.1. Mimicking the Klausmeier model: sticky-soil reduction of the unification model

Applying the sticky-soil assumption $d_2 = 0$ (Section 2.1.2), the unification model (6) can be formally reduced by computing

$$W_{\text{st}} = \frac{r_2 HB}{r_1 B(1+\eta B) + l_2};$$

the reduced model is then given by

$$\begin{cases} H_t &= d_1\Delta H &-l_1 H &+p &-r_2 HB \\ B_t &= d_3\Delta B &-l_3 B & &+jr_2 HB\frac{r_1 B(1+\eta B)}{r_1 B(1+\eta B)+l_2} \end{cases}$$

which is reminiscent of the Klausmeier model (11) as it provides a way how linear infiltration and uptake processes (for $\eta = 0$) can combine into a quadratic function (12). Indeed, for positive l_2, B is self-activating (also now for $\eta = 0$) since in a positive spatially homogeneous steady state:

$$\frac{\partial}{\partial B}\left[-l_3 B + jr_2 HB\frac{r_1 B(1+\eta B)}{r_1 B(1+\eta B)+l_2}\right] = B\frac{\partial}{\partial B}\left[\frac{jr_1 r_2 HB(1+\eta B)}{r_1 B(1+\eta B)+l_2}\right] = \frac{jl_2 r_1 r_2 HB(1+2\eta B)}{(r_1 B(1+\eta B)+l_2)^2} > 0.$$

Pivotal is that soil water loss is not a linear function of biomass B (namely constant); in the Gilad model [12], soil water evaporation is decreasing with B, which would strengthen the self-activation.

Comparison of bifurcating Turing patterns in the unification model between default parameters ($d_2 = 100$) and the sticky soil limit ($d_2 = 0$) is shown in Figs. 4 and 5.

Table 1
Inferred parameter values for the unification model from the literature; chosen values in the right column. Note that in [19] parameters are expressed in gram, day and millimeter, which have been replaced by kilogram, years and kilogram per square meter respectively. The values of r_1 and r_2 are derived from the Rietkerk (and Gilad for r_2) model by computing the slope of the uptake and infiltration function at $W = 0$ and $B = 0$ respectively, see (18).

Parameter	Unit	Klausmeier [6]	Rietkerk [19]	Simplified Gilad [12]|[24]		This article
d_1	m^2/yr	500[a]	36 500	–[b]	–[b]	10 000 (or 0)
d_2	m^2/yr	–	36.5	0.0625	2.5	100 (or 0)
d_3	m^2/yr	1	36.5	0.000625	0.1	1
l_1	1/yr	4	0	0	4.5	0 or 1
l_2	1/yr	–	73	4	1.5	1
l_3	1/yr	1.8	91.25	1.2	2	1
r_1	m^2/(kg yr)	–	3650	20	14	1
r_2	m^2/(kg yr)	–	11 680	720	99	1 (or ∞)
j	1	0.003	0.01	0.0016	0.0021	0.01
η	m^2/kg	0	0	3.5	1.5	0 or 1
q	1	–	–	2	2	1

[a]Taken from [14].
[b]No corresponding parameter in the Gilad model because, there, water diffuses nonlinearly.

4. The Rietkerk model

Introduced in [11,19], the Rietkerk model is given by (1) with

$$\begin{cases} I_R(B) = & \frac{B+k_2 w_0}{B+k_2} \\ U_R(W,B) = & \frac{WB}{W+k_1} \\ l_1 = & 0 \end{cases} \tag{13}$$

so explicitly:

$$\begin{cases} H_t & = d_1 \Delta H & +p & -\tilde{r}_2 H \frac{B+k_2 w_0}{B+k_2} & \\ W_t & = d_2 \Delta W & -l_2 W & +\tilde{r}_2 H \frac{B+k_2 w_0}{B+k_2} & -\tilde{r}_1 \frac{WB}{W+k_1} \\ B_t & = d_3 \Delta B & -l_3 B & & +j\tilde{r}_1 \frac{WB}{W+k_1} \end{cases}$$

with original parameter values in Table 1 and

$$\tilde{r}_1 = 18\,250\,\frac{1}{\text{yr}},\ \tilde{r}_2 = 73\,\frac{1}{\text{yr}},\ w_0 = 0.2,\ k_1 = 5\,\frac{\text{kg}}{\text{m}^2},\ k_2 = 0.005\,\frac{\text{kg}}{\text{m}^2}, \tag{14}$$

where we used that a liter of water is equivalent to 1 mm of rainfall per square meter, which weighs a kilogram.

The only positive spatially homogeneous steady state (for $l_3 < j\tilde{r}_1$ and $p > \frac{k_1 l_2 l_3}{j\tilde{r}_1 - l_3}$) is

$$(H_+, W_+, B_+) = \left(\frac{p}{\tilde{r}_2} \frac{B_+ + k_2}{B_+ + k_2 w_0}, \frac{k_1 l_3}{j\tilde{r}_1 - l_3}, \frac{j}{l_3}\left(p - \frac{k_1 l_2 l_3}{j\tilde{r}_1 - l_3}\right)\right),$$

where H_+ is expressed as a function of B_+. The Jacobian of the reaction terms is given by

$$A = \begin{pmatrix} -\tilde{r}_2 \frac{B+w_0 k_2}{B+k_2} & 0 & -\tilde{r}_2 H k_2 \frac{1-w_0}{(B+k_2)^2} \\ \tilde{r}_2 \frac{B+w_0 k_2}{B+k_2} & -l_2 - \frac{\tilde{r}_1 k_1 B}{(W+1)^2} & \tilde{r}_2 H k_2 \frac{1-w_0}{(B+k_2)^2} - \frac{\tilde{r}_1 W}{W+k_1} \\ 0 & \frac{j\tilde{r}_1 k_1 B}{(W+1)^2} & -l_3 + \frac{j\tilde{r}_1 W}{W+k_1} \end{pmatrix}$$

and evaluated in (H_+, W_+, B_+) this becomes

$$A_+ = \begin{pmatrix} -\tilde{r}_2 \frac{B_+ + w_0 k_2}{B_+ + k_2} & 0 & -\frac{pk_2}{B_+ + k_2 w_0} \frac{1-w_0}{B_+ + k_2} \\ \tilde{r}_2 \frac{B_+ + w_0 k_2}{B_+ + k_2} & -l_2 - \frac{\tilde{r}_1 k_1 B_+}{(W_+ + 1)^2} & \frac{pk_2}{B_+ + k_2 w_0} \frac{1-w_0}{B_+ + k_2} - \frac{l_3}{j} \\ 0 & \frac{j\tilde{r}_1 k_1 B_+}{(W_+ + 1)^2} & 0 \end{pmatrix} \tag{15}$$

so that

$$\begin{aligned} \text{tr}(A_+) &= -\tilde{r}_2 \frac{B_+ + w_0 k_2}{B_+ + k_2} - l_2 - \frac{\tilde{r}_1 k_1 B_+}{(W_+ + 1)^2} < 0, \\ \det(A_+) &= -\frac{\tilde{r}_1 \tilde{r}_2 k_1 l_3 B_+}{(W_+ + 1)^2} \frac{B_+ + w_0 k_2}{B_+ + k_2} < 0. \end{aligned}$$

Thus, (H_+, W_+, B_+) is stable against spatially homogeneous perturbations if and only if the Routh–Hurwitz criterion is satisfied (confer (10)):

$$\beta_0(0) + \beta_1(0)\beta_2(0) = \det(A_+) - \text{tr}(A_+)(A_{1,1} + A_{2,2} + A_{3,3}) > 0. \tag{16}$$

From (15) we can read off that $a_{11}, a_{22} < 0$, $a_{33}, A_{2,2} = 0$ and $A_{3,3} > 0$, so (H_+, W_+, B_+) is not Turing–Hopf unstable (by Lemma 2 since $d_1 \geq d_2, d_3$). The only option for Turing instability is if $A_{1,1} < 0$ (confer Lemma 1). It holds that

$$A_{1,1} = \frac{\tilde{r}_1 k_1 B_+}{(W_+ + 1)^2}\left(l_3 - \frac{jpk_2}{B_+ + k_2 w_0}\frac{1-w_0}{B_+ + k_2}\right)$$

which is negative if

$$l_3 < \frac{jpk_2}{B_+ + k_2 w_0}\frac{1-w_0}{B_+ + k_2}. \tag{17}$$

If $p \downarrow \frac{k_1 l_2 l_3}{j\tilde{r}_1 - l_3}$ then $B_+ \downarrow 0$, and (17) reduces to

$$k_2 w_0 (j\tilde{r}_1 - l_3) < j k_1 l_2 (1 - w_0).$$

This inequality is satisfied by the original choice of parameter values (14), so Turing instability can (indeed) occur.

4.0.1. Sandy and sticky soil; reduction to two components

The sandy-soil setting ($d_1 = 0$, Section 2.1.1) applied to the Rietkerk model does not exhibit Turing patterns since $-d_1 A_{1,1}$ is the only negative term in $\beta_0(k)$ (9). From another viewpoint, in the sandy-soil reduced system B is not self-activating ($a_{33} = 0$ in (15)) and Turing instability moreover is a priori impossible for $d_2 = d_3 = 0.1$ (Table 1). For the sticky-soil assumption ($d_2 = 0$) and subsequent reduction (Section 2.1.2), this is not as easy to compute and therefore omitted: it was determined for the simpler unification model in Section 3.1. Note that for the computation in Fig. 2, there was no visual distinction between $d_2 = 0.1$ and $d_2 = 0$, so in this case Turing instability is preserved in the sticky-soil limit. In [33], soil water diffusion was also neglected as no significant differences were noticed.

4.0.2. Including surface water evaporation

Changing the Rietkerk model by allowing for surface water evaporation $l_1 > 0$, as in [34], there may be two positive spatially homogeneous steady states of the Rietkerk model, given by

$$\begin{cases} H_\pm & = \frac{jl_2 W_\pm + l_3 B_\pm}{j\tilde{r}_2} \frac{B_\pm + k_2}{B_\pm + k_2 w_0} \\ W_\pm & = \frac{k_1 l_3}{j\tilde{r}_1 - l_3} \\ B_\pm & = B_{\text{fold}} \pm \sqrt{B_{\text{fold}}^2 - \frac{jk_2}{l_3}\frac{\tilde{r}_2 w_0 (p - l_2 W_\pm) - l_1 l_2 W_\pm}{\tilde{r}_2 + l_1}} \end{cases}$$

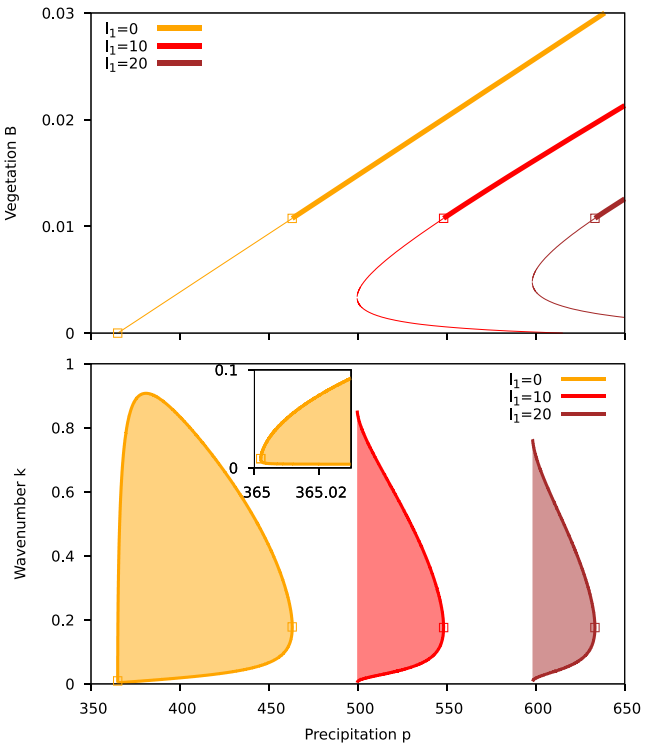

Fig. 2. Rietkerk model with and without surface water evaporation l_1, using parameter values from Table 1 and (14). Top panel: vegetation component $B_\pm$ of positive spatially homogeneous steady states, with squares at the loci where (H_+, W_+, B_+) becomes Turing unstable. Stability is indicated by thick curves. Bottom panel: range of wavenumbers k against which (H_+, W_+, B_+) is Turing unstable. For $l_1 = 0$, the Turing instability at low precipitation p results from instability against small wavenumbers. For larger l_1 this Turing instability is lost but the Turing instability at larger p persists (as long as l_1 does not become too large). No Turing–Hopf unstable wavenumbers were encountered. Changing $d_2 = 0.1$ into $d_2 = 0$ does not have any significant impact.

where

$$B_{\text{fold}} = \frac{\tilde{r}_2(jp - jl_2W_\pm + k_2l_3w_0) - jl_1l_2W_\pm - k_2l_1l_3}{2l_3(\tilde{r}_2 + l_1)}.$$

Further analytical analysis is not attempted, the Turing instability of (H_+, W_+, B_+) is shown for $l_1 = 0$, $l_1 = 10$ and $l_1 = 20$ in Fig. 2. For $l_1 > 0$ the spatially homogeneous solution starts to fold back and the boundary of the region of Turing unstable modes in the (p, k)-plane no longer consists solely of marginally (un)stable modes.

4.1. Mimicking the Rietkerk model: the unification model with $\eta = 0$

The unification model with $\eta = 0$ is a multi-linear Rietkerk model in the following sense. The infiltration function in the Rietkerk model I_R can be approximated by the linear function $I(B) = B$. The uptake function U_R can be approximated by the multi-linear (mass action) function $U(W, B) = WB$. The corresponding rate parameters are chosen:

$$\begin{aligned} r_1 &= \tilde{r}_1 \tfrac{\partial}{\partial W}\left[\tfrac{U_R}{B}\right]\Big|_{W=0} &&= \tfrac{\tilde{r}_1}{k_1}, \\ r_2 &= \tilde{r}_2 \tfrac{\partial}{\partial B}[I_R]\big|_{B=0} &&= \tilde{r}_2 \tfrac{1-w_0}{k_2}. \end{aligned} \tag{18}$$

By replacing U_R and I_R by U and I respectively, we obtain the unification model (6) with $\eta = 0$:

$$\begin{cases} H_t &= d_1\Delta H &-l_1H &+p &-r_2HB & \\ W_t &= d_2\Delta W &-l_2W & &+r_2HB &-r_1WB \\ B_t &= d_3\Delta B &-l_3B & & &+jr_1WB. \end{cases} \tag{19}$$

The positive homogeneous steady states of (19), for $p \geq \frac{l_3}{j}\left(\frac{l_1}{r_2} + \frac{l_2}{r_1} + 2\sqrt{\frac{l_1l_2}{r_1r_2}}\right)$, are given by:

$$\begin{cases} H_\pm &= \frac{l_3}{jr_2}\left(1 + \frac{l_2}{r_1B_\pm}\right) \\ W_\pm &= \frac{l_3}{jr_1} \\ B_\pm &= \frac{1}{2}\left(\frac{jp}{l_3} - \frac{l_1}{r_2} - \frac{l_2}{r_1}\right) \pm \sqrt{\frac{1}{4}\left(\frac{jp}{l_3} - \frac{l_1}{r_2} - \frac{l_2}{r_1}\right)^2 - \frac{l_1l_2}{r_1r_2}} \end{cases}$$

where B_- is only positive if $l_1 > 0$. Substituting this in the Jacobian of the reaction terms (7), with $\eta = 0$, yields:

$$A_\pm = \begin{pmatrix} -l_1 - r_2B_\pm & 0 & -\frac{l_3}{j}\left(1 + \frac{l_2}{r_1B_\pm}\right) \\ r_2B_\pm & -l_2 - r_1B_\pm & \frac{l_2l_3}{jr_1B_\pm} \\ 0 & jr_1B_\pm & 0 \end{pmatrix}. \tag{20}$$

4.1.1. Sandy and sticky soil; reduction to two components

For the same reasons as mentioned for the Rietkerk model in Section 4.0.1, the sandy soil limit $d_1 = 0$ does not yield Turing patterns. The sticky-soil reduction was determined in 3.1, showing that vegetation B is self-activating. A comparison of the unification model with default parameter value, $d_2 = 100$, and sticky soil, $d_2 = 0$, is presented in Fig. 4.

Remark. Note that vegetation B has become self-activating only after sticky-soil reduction: B is not self-activating in (the unification model mimicking) the Rietkerk model ($a_{33} = 0$ in (15) and (20)). Despite this, B is sometimes referred to as 'activator' in the Rietkerk model in the literature [3,34].

4.1.2. Turing patterns

We first look into stability of the spatially homogeneous steady states against spatially homogeneous perturbations. It holds that

$$\begin{aligned} \operatorname{tr}(A_\pm) &= -l_1 - l_2 - (r_1 + r_2)B_\pm < 0, \\ \det(A_\pm) &= l_3(l_1l_2 - r_1r_2B_\pm^2), \end{aligned}$$

and $\operatorname{sign}(\det(A_\pm)) = \mp 1$ so (H_-, W_-, B_-) is unstable against spatially homogeneous perturbations. Now (H_+, W_+, B_+) is stable against these perturbations if and only if the Routh–Hurwitz criterion (16) holds, with

$$\begin{aligned} &A_{1,1} = -l_2l_3 < 0, \\ &A_{2,2} = 0, \\ &A_{3,3} = (l_1 + r_2B_+)(l_2 + r_1B_+) > 0. \end{aligned}$$

If $\eta = 0$, $l_1 \geq l_3$ and $d_1 \geq d_2, d_3$, then it does hold:

$$\begin{aligned} \beta_0(0) + \beta_1(0)\beta_2(0) &= l_3(l_1l_2 - r_1r_2B_+^2) + (l_1 + l_2 + (r_1 + r_2)B_+) \\ &\quad \times ((l_1 + r_2B_+)(l_2 + r_1B_+) - l_2l_3) \\ &> l_3(l_1l_2 - r_1r_2B_+^2) + (l_1 + l_2 + (r_1 + r_2)B_+) \\ &\quad \times l_3r_1B_+ > 0. \end{aligned} \tag{21}$$

Since B_+ is invariant under a change of parameters $(l_3, p) \mapsto (\delta l_3, \delta p)$, it is easy to see that the criterion holds if δ is small and fails if δ is large.

Next we view the stability of (H_+, W_+, B_+) against spatially heterogeneous perturbations. Since $a_{11}, a_{22} < 0$, $a_{33}, A_{2,2} = 0$ and $A_{3,3} > 0$, it can only be stationary Turing unstable, through $A_{1,1} < 0$ (confer Lemmas 1 and 2). The signs of the elements of A_+, and their roles in Turing pattern formation, are graphically represented in the left panel of Fig. 3. In Fig. 4, a comparison of Turing instability for $d_2 = 100$ (default) and $d_2 = 0$ (sticky soil, Section 2.1.2) of the unification model with $\eta = 0$ is shown. Turing pattern formation is preserved; with soil water flux ($d_2 = 100$)

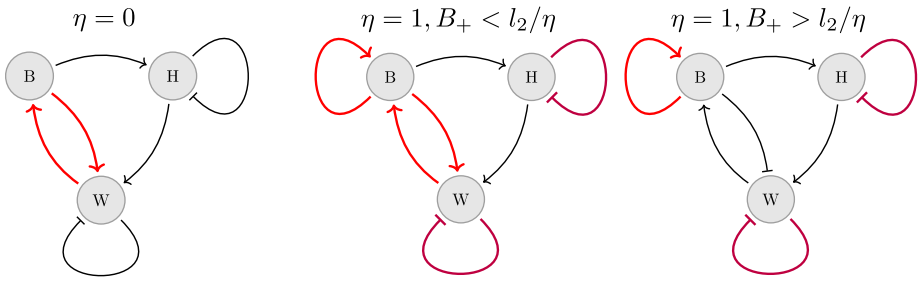

Fig. 3. Depiction of processes involved in Turing(-Hopf) instability in the unification model for $\eta = 0$ (left diagram) and $\eta = 1$ (middle and right diagram). If, in response to a marginal increase of component X, component Y increases, then this is represented by $X \to Y$ (activation). If instead the response in negative, this is represented by $X \dashv Y$ (inhibition). Left: the mutual activation $W \leftrightarrow B$ (component 2 resp. 3) causes $A_{1,1} < 0$. If (17) holds, the Rietkerk model corresponds to this situation. Note that there is no arrow from B to itself, so vegetation is not self-activating: $a_{33} = 0$. Middle: as for $\eta = 0$, $A_{1,1} < 0$ because $B \leftrightarrow W$, but here also the self-activation of B combined with the self-inhibition of W contributes. In addition, $a_{33} > 0$ ($B \to B$) and $A_{2,2} < 0$ ($B \to B$ together with $H \dashv H$). Right: Still $A_{1,1} < 0$, although B now inhibits W. Also still $a_{33} > 0$ and $A_{2,2} < 0$.

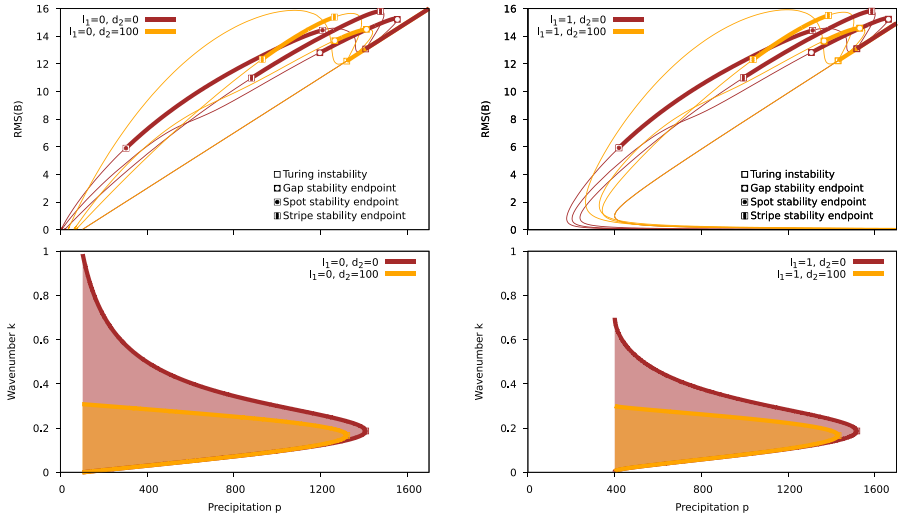

Fig. 4. Turing patterns in the unification model, using default parameters (Table 1) with $\eta = 0$, compared to using the same parameters except $d_2 = 0$ (sticky-soil limit, Section 2.1), for $l_1 = 0$ (left) and $l_1 = 1$ (right). Top panels: root mean square (RMS) of the vegetation component B of selection of steady states as a function of precipitation p. Stability on the domain Ω is indicated by thick lines. Stable homogeneous states enter top right and become Turing unstable, giving rise to gap, spot and stripe patterns. The stability of the steady states in the reduced sticky-soil two-component models is identical to those in the three-component models with $d_2 = 0$. Only the spot patterns for $d_2 = 100$ are unstable for all p (on Ω); the bifurcation structure is well-preserved in the sticky-soil limit. Bottom panels: range of wavenumbers k against which (H_+, W_+, B_+) is Turing unstable. By Lemma 2, homogeneous steady states cannot be Turing–Hopf unstable. For $l_1 = 1$, by (21), there are no wavenumbers k against which (H_+, W_+, B_+) is Turing–Hopf unstable. For $l_1 = 0$, tiny insignificant ranges of Turing–Hopf unstable wavenumbers exist (not shown).

spots with critical wavelength are always unstable whereas without soil water flux ($d_2 = 0$) spots are stable for a range of precipitation p (on Ω). Furthermore, the presence of surface water evaporation l_1 shifts the solution branches for large p and introduces folds for small p.

Remark. Mutual activation of W and B, e.g. as in the left panel of Fig. 3, can be transformed into a mutual inhibition by replacing W by $P - W$, as in Fig. A.8. So this driving mechanism of Turing pattern formation is equivalent to the "inhibition of an inhibition" [35], which is also prevalent in [36].

5. Simplified Gilad model

In the Gilad model, as in the Rietkerk model, it is assumed that surface water evaporation is negligible: $l_1 = 0$ (except in [37]). From [24], without imposing a bound on the biomass ($K = \infty$), the flat Gilad model is given by:

$$\begin{cases} \frac{\partial}{\partial t}H &= d_1\Delta H^2 &+p &-\tilde{r}_2 H \cdot I_R(B) & \\ \frac{\partial}{\partial t}W &= d_2\Delta W &-l_2 W &+\tilde{r}_2 H \cdot I_R(B) &-G_W W \\ \frac{\partial}{\partial t}B &= d_3\Delta B &-l_3 B & &+G_B B \end{cases} \tag{22}$$

with infiltration I_R identical to the Rietkerk model (13) and

$$G_W(\mathbf{x}) = r_1 \int_\Omega G(\mathbf{y}, \mathbf{x}) B(\mathbf{y}) d\mathbf{y},$$
$$G_B(\mathbf{x}) = j r_1 \int_\Omega G(\mathbf{x}, \mathbf{y}) W(\mathbf{y}) d\mathbf{y},$$

where $G(\mathbf{x}, \mathbf{y}) = \frac{1}{2\pi S_0^2} \exp\left(-\frac{|\mathbf{x}-\mathbf{y}|^2}{2\,(S_0(1+\eta B(\mathbf{x})))^2}\right).$

By taking a limit of the lateral extent of the roots S_0 to zero, the nonlocal terms can be replaced by local ones [20]. It holds that

$$\begin{aligned} \lim_{S_0 \to 0} G_W(\mathbf{x}) &= r_1 B(\mathbf{x})(1+\eta B(\mathbf{x}))^2; \\ \lim_{S_0 \to 0} G_B(\mathbf{x}) &= j r_1 W(\mathbf{x})(1+\eta B(\mathbf{x}))^2, \end{aligned} \tag{23}$$

see Appendix B for computational details. Together with the replacement of nonlinear by linear surface water diffusion (which in the Klausmeier model does not seem to make a qualitative difference [31]), (22) simplifies to

$$\begin{cases} \frac{\partial}{\partial t}H &= d_1\Delta H &+p &-\tilde{r}_2 H \cdot I_R(B) & \\ \frac{\partial}{\partial t}W &= d_2\Delta W &-l_2 W &+\tilde{r}_2 H \cdot I_R(B) &-r_1 U \\ \frac{\partial}{\partial t}B &= d_3\Delta B &-l_3 B & &+j r_1 U \end{cases} \tag{24}$$

with uptake

$U(W,B) = WB(1+\eta B)^2$.

Now (24) fits the framework (1).

5.0.1. Sandy and sticky soil; reduction to two components

After applying the sandy-soil reduction (Section 2.1.1), the Jacobian of the reaction terms becomes

$$A = \begin{pmatrix} -l_2 - r_1 B(1+\eta B)^2 & -r_1 W(1+4\eta B+3\eta^2 B^2) \\ j r_1 B(1+\eta B)^2 & -l_3 + j r_1 W(1+4\eta B+3\eta^2 B^2) \end{pmatrix}$$

where evaluation of a_{22} in a positive spatially homogeneous state (W_+, B_+) shows that B is self-activating:

$a_{22}(W_+, B_+) = 2 j r_1 W_+ \eta B_+ (1+\eta B_+) > 0.$

This has been utilized in [20]. For determining the sticky-soil reduction (Section 2.1.2):

$$W_{\mathrm{st}} = \frac{\tilde{r}_2 H \cdot I_R}{B(1+\eta B)^2 + l_2}$$

which (depending on parameters) after substitution in U does yield a two-component Turing system. Resulting Turing patterns of a simplified Gilad representative in the unification model are computed next.

5.1. Mimicking the simplified Gilad model: the unification model for $\eta = 1$

Replacing I_R in (24) by I, as in Section 4.1, we obtain the unification model (6) with $q = 2$. To view the lowest order correction to the model with $\eta = 0$, we replace $q = 2$ by $q = 1$. We also take into account surface water evaporation: $l_1 \geq 0$.

In this case, the two positive spatially homogeneous steady states of (6) are given by:

$$\begin{cases} H_\pm &= \frac{l_3}{j r_2}\left(1 + \frac{l_2}{r_1 B_\pm (1+\eta B_\pm)}\right) \\ W_\pm &= \frac{l_3}{j r_1 (1+\eta B_\pm)} \end{cases}$$

with $B_\pm$ the solutions of

$$\begin{aligned} &j p r_1 r_2 B_\pm (1+\eta B_\pm) - l_3 \left(l_1 \left(l_2 + r_1 B_\pm (1+\eta B_\pm)\right)\right) \\ &\quad + r_2 B_\pm \left(l_2 + r_1 B_\pm (1+\eta B_\pm)\right) = 0 \end{aligned}$$

for p sufficiently large.

The Jacobian of the reaction terms evaluated in $(H_\pm, W_\pm, B_\pm)$ is

$$A_\pm = \begin{pmatrix} -l_1 - r_2 B_\pm & 0 & -\frac{l_3}{j}\left(1 + \frac{l_2}{r_1 B_\pm (1+\eta B_\pm)}\right) \\ r_2 B_\pm & -l_2 - r_1 B_\pm (1+\eta B_\pm) & \frac{l_3}{j r_1}\frac{l_2 - \eta B_\pm}{B_\pm (1+\eta B_\pm)} \\ 0 & j r_1 B_\pm (1+\eta B_\pm) & \frac{l_3 \eta B_\pm}{1+\eta B_\pm} \end{pmatrix} \tag{25}$$

so that

$$\begin{aligned} \mathrm{tr}(A_\pm) &= -l_1 - l_2 - r_2 B_\pm - r_1 B_\pm (1+\eta B_\pm) + \tfrac{l_3 \eta B_\pm}{1+\eta B_\pm}, \\ \det(A_\pm) &= a_{11} A_{1,1} + l_3 \left(l_1 (l_2 + \eta B_\pm) - r_2 B_\pm^2 (r_1 + \eta + r_1 \eta B_\pm)\right), \end{aligned}$$

where $\mathrm{sign}(\det(A_\pm)) = \mp 1$ so (H_-, W_-, B_-) is unstable against spatially homogeneous perturbations. Note that again $(H_\pm, W_\pm, B_\pm)$ is invariant under a parameter transformation $(l_3, p) \mapsto (\delta l_3, \delta p)$, so $\mathrm{tr}(A_+)$ can both be positive (for large δ) and negative (for small δ). Apart from the sign of the trace, stability of (H_+, W_+, B_+) depends on fulfillment of (16).

5.1.1. Sandy and sticky soil; reduction to two components

Since $a_{33} > 0$ (25), the sandy-soil reduced system (Section 2.1.1) does satisfy the self-activation condition for being a Turing model (Appendix A.1). The sticky-soil reduction was already determined in Section 3.1. Comparison of Turing patterns for various parameter settings is presented in Fig. 5.

5.1.2. Turing patterns

From (25) we can read off that $a_{11}, a_{22} < 0$, $a_{33} > 0$,

$$\begin{aligned} A_{1,1} &= -l_2 l_3 \left(1 + \tfrac{\eta B_+}{1+\eta B_+}\right) < 0, \\ A_{2,2} &= -(l_1 + r_2 B_+)\tfrac{l_3 \eta B_+}{1+\eta B_+} < 0, \\ A_{3,3} &= (l_1 + r_2 B_+)(l_2 + r_1 B_+ (1+\eta B_+)) > 0. \end{aligned}$$

So Turing(-Hopf) instability can be caused by $a_{33} > 0$, $A_{1,1} < 0$ as well as $A_{2,2} < 0$ (confer Lemmas 1 and 2). This is graphically represented in Fig. 3.

In Fig. 5, Turing patterns are shown for both the default parameter setting ($d_1 = 10000$, $d_2 = 100$), the sandy soil limit ($l_1 = d_1 = 0$) and the sticky-soil limit ($d_2 = 0$), for the unification model with $\eta = 1$. Again, Turing–Hopf unstable modes do not play a (significant) role, and the range of stability of the steady states in the reduced two-component systems is identical to those in the corresponding three-component system. Just like for $\eta = 0$, the qualitative bifurcation structure near Turing is preserved when changing from default ($d_2 = 100$) to sticky soil ($d_2 = 0$); what stands out is that both the stripes and spots gain a range of stability for $d_2 = 0$ in comparison to $d_2 = 100$. The change from $d_1 = 10000$ to the sandy-soil limit $d_1 = 0$ is more drastic: Turing bifurcation occurs at much smaller precipitation p, with stripes bifurcating supercritically instead of subcritically, and it exhibits a stable range of spots instead of gaps. What also makes the bifurcating Turing patterns in this sandy-soil limit stand out from all the other pattern bifurcation plots, is that the branches return to the spatially homogeneous solution at the black cross. This scenario can already be read off from the orange range of Turing unstable wavenumbers, since the orange curve of Turing marginally unstable modes attains the value $k = k_c$ twice, namely at the orange square indicating the Turing instability and at the black cross.

As observed for $\eta = 0$, changing the surface water evaporation rate from $l_1 = 0$ to $l_1 = 1$ only constitutes a shift for large precipitation p, at small p branches fold for $l_1 = 1$. In comparison to $\eta = 0$ (Fig. 4), for $\eta = 1$ the spots still bifurcate supercritically but only after two or four folds the branch arrives at small p (except for $d_1 = 0$). Furthermore, Turing patterns form at lower p for $\eta = 1$ than for $\eta = 0$.

6. Turing–Hopf instability: three versus two components

Until now, the range of stability of steady states in the sandy-soil ($l_1 = d_1 = 0$) and sticky-soil ($d_2 = 0$) limit did not depend on whether a subsequent reduction to a two-component system was performed. Here we deviate slightly from the parameter values in Table 1 by choosing slow infiltration $r_2 = 0.1$ and $\eta \in \{0, 0.25, 0.5, 1\}$, and study the three-component unification model in the sandy soil limit ($l_1 = d_1 = 0$). From an ecological perspective it makes more sense to study the reduced two component model (Section 2.1.1) and sandy soil would rather imply $r_2 \gg 1$; the results below are mainly meant to illustrate how the dynamics of the two- and three-component model can be different (even though the steady states are equal). In particular, in a two-component system a spatially homogeneous steady state cannot be Turing–Hopf unstable (Appendix A.1).

The Turing(-Hopf) unstable modes are shown in Fig. 6. For $\eta \in \{0, 0.25\}$, there are no Turing unstable modes. For $\eta \in \{0.5, 1\}$,

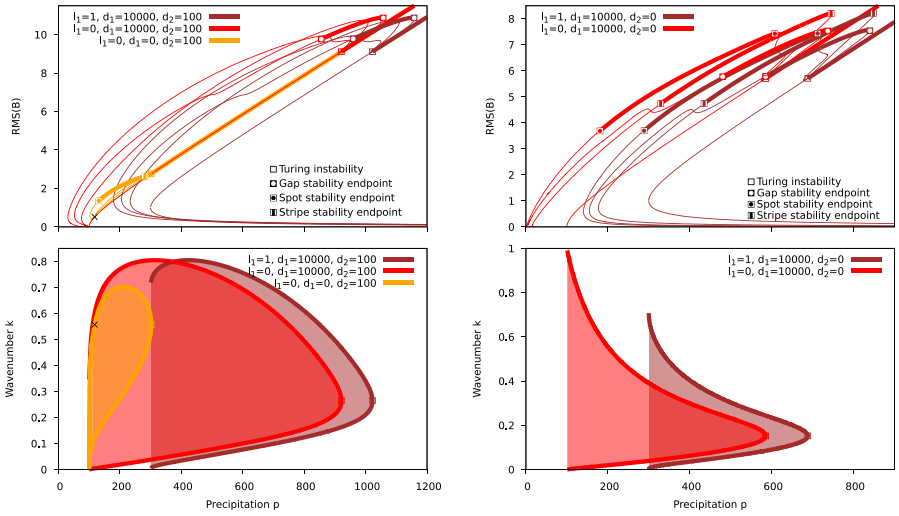

Fig. 5. Reductions of the unification model mimicking the simplified Gilad model, using the parameters from Table 1 and $\eta = r_2 = 1$. Top panels: root mean square (RMS) of the vegetation component B of a selection of steady states as a function of precipitation p. Stability on the domain Ω is indicated by thick lines. Stable homogeneous states enter top right and become Turing unstable, giving rise to gap, spot and stripe patterns. Bottom panels: range of wavenumbers k against which (H_+, W_+, B_+) is Turing unstable. For $l_1 = 0$ tiny ranges of Turing–Hopf unstable wavenumbers exist (not shown), but only within the range of precipitation p where (H_+, W_+, B_+) is already Turing unstable. Left: (un)stable steady states of the unification model with $l_1 = d_1 = 0$ (see (3), in orange), in this case stability is identical to stability in the sandy-soil reduced two-component system (2); both the spots and stripes bifurcate stably on Ω and the gaps are always unstable; the branches converge back to the spatially homogeneous state at the second solution of $\beta_0(k_c) = 0$ (see (9)). For $d_1 = 10000$ (and $l_1 = 0$ or 1), only the gaps (with critical wavenumber) are stable on Ω for a range of p. Right: (un)stable steady states of the unification model with $d_2 = 0$, again stability is identical to stability in the (sticky-soil) reduced two-component system (4); all patterns are stable (on Ω) for a range of p-values. (For interpretation of the references to color in this figure legend, the reader is referred to the web version of this article.)

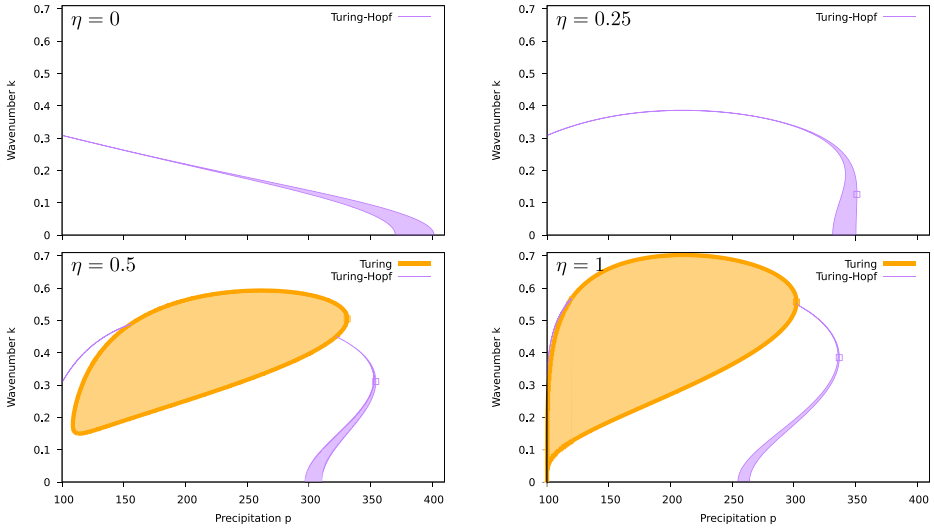

Fig. 6. Range of wavenumbers k against which (H_+, W_+, B_+) is Turing(-Hopf) unstable in the unification model with $l_1 = d_1 = 0$ (sandy soil) and $r_2 = 0.1$ for $\eta = 0, 0.25, 0.5, 1$. Squares indicate the loci where (H_+, W_+, B_+) becomes Turing(-Hopf) unstable. In the two-component sandy-soil reduced system the Turing unstable modes all persist but the Turing–Hopf unstable modes all disappear. Top left: $\eta = 0$. There are no Turing unstable modes. The homogeneous steady state, for decreasing precipitation p, first becomes Hopf unstable against a spatially homogeneous mode $k = 0$. Top right: $\eta = 0.25$. A Turing–Hopf instability appears. Bottom left: $\eta = 0.5$. Turing–Hopf unstable modes and Turing instability appear. The Turing instability is preceded by the Turing–Hopf instability (for decreasing p). The range of Turing unstable wavenumbers and Turing–Hopf unstable wavenumbers (e.g. orange and purple region respectively) are disjoint (Lemma 3): the region of Turing–Hopf unstable modes is split in two. Bottom right: $\eta = 1$. Turing unstable modes coincide with Turing unstable modes in bottom left panel of Fig. 5. (For interpretation of the references to color in this figure legend, the reader is referred to the web version of this article.)

there are Turing unstable modes but, for decreasing precipitation p, the Turing instability is preceded by a Turing–Hopf instability. In the corresponding reduced two-component system, no Turing–Hopf unstable modes exist and all the Turing unstable modes persist: the spatially homogeneous steady state would be destabilized by the Turing instability.

Time-integration of the unification model for $\eta = 1$, with $p = 330$ in the range of Turing–Hopf instability (Fig. 6), shows the formation of rotating spiral patterns, in Fig. 7. A heuristic explanation is that, as $l_1 = d_1 = 0$, resource (surface water) accumulates at locations without vegetation. Neighboring vegetation can spread toward such a location, deplete the resource, and 'move' toward a next location. Then the build-up of resources can start again. Obviously, with the resource being surface water this is not a realistic scenario and the corresponding two-component reduced model (without surface water component) – which does not have this Turing–Hopf instability – was the more logical one to choose anyways.

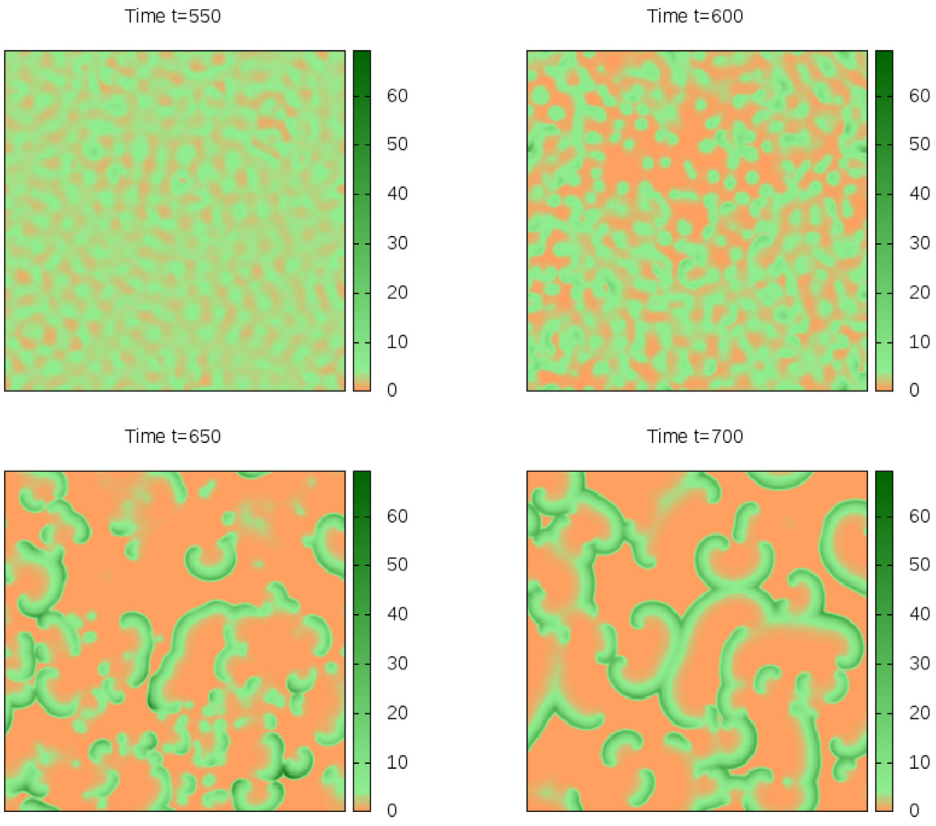

Fig. 7. Simulation of the unification model with $p = 330$, $\eta = 1$, $r_2 = 0.1$ and $l_1 = d_1 = 0$. The spatially homogeneous steady state is not Turing unstable but Turing–Hopf unstable (Fig. 5). Domain size 100×100 with periodic boundary conditions. As time progresses, moving patterns start to grow that eventually develop into (pairs of) rotating spirals.

Notably, spiral vegetation patterns have been reported recently in highlands in arid conditions on the border of wetlands in Chile [38] and in Morocco and Bolivia [39]. Formation of spirals within the Rietkerk model, out of a pattern of stripes instead of a spatially homogeneous state, was reported for a particular parameter combination in [25].

7. Implications for model selection

The Klausmeier, Rietkerk and Gilad models have been successful in qualitatively reproducing observed spatially periodic vegetation patterns. On a fundamental level, the different models produce the same outcome (referred to as equifinality) and the challenge is to use observations to discriminate between alternate explanatory mechanisms [40]. In this article the Rietkerk and simplified Gilad model were represented within a unification model, and the Klausmeier model was approximated by reduction of the unification model. The unification model is a minimal model that focuses on processes that drive vegetation pattern formation: infiltration is a linear function of surface water and vegetation; uptake is linear in soil water and linear or quadratic in vegetation, replacing more refined nonlinear functions in the Rietkerk and simplified Gilad model. This allowed the identification of drivers of Turing pattern formation in different models.

Model selection could be based on measuring these drivers using field experiments, but there are some challenges. Precipitation in drylands is intermittent, though in the models it varies on the climatic time scale (see e.g. [33,41–44] for model studies with seasonality/intermittency). If the real-world process is linear, average precipitation may suffice as model input. But, for instance, the spreading speed of surface water depends on rain shower intensity and this process is represented in models by a constant diffusion constant d_1. In this case measurements of an intermittent nonlinear process need to be translated into some (weighted) average that can be used in the model.

Notwithstanding these issues, based on field measurements it might be possible to determine whether in response to a marginal increase in vegetation, the marginal increase in surface water infiltration is larger than the marginal increase in soil water uptake. In all models, this is exactly what leads to the first principal minor $A_{1,1}$ being negative, which is the only driver of Turing instability in (the representative mimicking) the Rietkerk model.

In (the representative mimicking) the simplified Gilad model, additionally vegetation is self-activating ($a_{33} > 0$), because uptake through the root network increases disproportionally with plant size. For individual plants, the uptake rate could be measured as a function of plant size. If patches of vegetation consist of multiple individual plants the interpretation becomes more challenging, since two plants at the same location may have equal biomass as a single larger plant, but a smaller combined root network.

In the literature and in this article, it has been tacitly assumed that the vegetation mortality rate is constant, and in this case auto-catalysis of the vegetation is equivalent to self-activation of the vegetation. Based on lower temperature measurements within vegetation [37], or by associational resistance to grazing [45], the mortality rate could be a decreasing function of vegetation. In this case vegetation may be self-activating without being auto-catalytic.

We found that the Klausmeier model can be approximated by sticky-soil reduction (no soil water flux) of the unification model, but there are some fundamental differences. For instance, in the

Klausmeier model, stripes generally bifurcate supercritically [31], in Fig. 4 and the top right panel of Fig. 5 they bifurcate subcritically. This is especially relevant since many of the (analytical) results in the literature are specific for supercritical bifurcations. The differences between the unification model with and without soil water diffusion were only minor: stripes and spots of critical wavenumber tended to gain stability without soil water diffusion, but for smaller wavenumber the situation may be different. Subsequent reduction to a two-component model did not change steady state stability in any of the cases.

Because vegetation is not self-activating in the Rietkerk model, in the sandy-soil limit (no surface water flux) Turing pattern formation disappears. For the unification model mimicking the Gilad model, Turing patterns are still present in the sandy-soil limit, but the changes are quite dramatic, indicating that surface water flux does play an important role for the default choice of parameter values. Subsequent reduction to a two-component model again did not change steady state stability, except for ecologically unrealistic parameters in Section 6.

In this article, the stability on a bounded domain Ω was computed for a selection of bifurcating patterns within a minimal model with largely unsubstantiated parameter values. These limited numerical continuation results leave some questions unanswered. As an example, the sandy-soil reduced model (without surface water flux) is the only model in this article with stripes and spots bifurcating stably on Ω (Fig. 5), not complying with the "standard sequence" [25], a difference that could be analyzed close-to-equilibrium e.g. by bifurcation analysis on a hexagonal lattice [46]. It would probably be a poor model to study "fairy circles" (gaps) in the Namibian sandy soil [47,48], since the model does not exhibit stable gaps with critical wavenumber. It is not clear what the pivotal (ecological) difference with the sandy-soil reduced simplified Gilad model [20] is, that results in the selection of gap patterns there.

A more refined analysis is needed for thorough comparison of model output. By applying numerical continuation techniques, representations of all stable patterns (Busse balloons) can be computed, which would provide a more solid basis for model comparison and can be tested against distributions of remotely sensed vegetation patterns [2,49–55].

Although steady states in three-component sandy/sticky models and those in the two-component reduced models are equal, they are more likely to be Hopf unstable in the three-component model and the dynamics might be different. In reaction–diffusion systems with advection, the anisotropy may cause patterns to move in a specific direction: in a comoving frame they would still be stationary. Turing–Hopf instability in isotropic systems (as in this article) results in movement in all possible directions, with patterns that are less regular than the steady states that generally arise after Turing instability. For application of advanced mathematical techniques, it is convenient to study the simplest model possible.

Declaration of competing interest

The authors declare that they have no known competing financial interests or personal relationships that could have appeared to influence the work reported in this paper.

Acknowledgments

The author thanks the Alexander von Humboldt Foundation for financial support, Ehud Meron and his research group for their hospitality and Hannes Uecker, Maarten Eppinga and two anonymous reviewers for valuable suggestions and comments.

Appendix A. Turing instability

Following the original article from Alan Turing [13], there have been numerous follow-up articles extending or reinterpreting this seminal work, see e.g. [56–63]. For easy reference, here some well-known properties of the Turing(-Hopf) instability in both two- and three-component reaction–diffusion systems are revisited.

A.1. Two-component Turing systems

A general two-component reaction–diffusion system without cross-diffusion is given by:

$$\begin{cases} u_t = & d_1 \Delta u + f(u, v) \\ v_t = & d_2 \Delta v + g(u, v). \end{cases} \tag{A.1}$$

The Jacobian of the reaction terms is given by:

$$A(u, v) := \begin{pmatrix} a_{11} & a_{12} \\ a_{21} & a_{22} \end{pmatrix} := \begin{pmatrix} \frac{\partial f}{\partial u} & \frac{\partial f}{\partial v} \\ \frac{\partial g}{\partial u} & \frac{\partial g}{\partial v} \end{pmatrix}.$$

We assume the existence of a spatially homogeneous solution $(\bar{u}, \bar{v})$ that is stable against spatially homogeneous perturbations ($\mathrm{tr}(A(\bar{u}, \bar{v})) < 0$ and $\det(A(\bar{u}, \bar{v})) > 0$). Since (A.1) is isotropic, we use k to denote the length of the wavevector of a periodic perturbation, i.e. in two spatial dimensions with wavevector (k_x, k_y), $k = \sqrt{k_x^2 + k_y^2}$, and refer to k as the wavenumber.

The dispersion relation is given by $\det(M - \lambda I) = 0$, where $M = A - Dk^2$ and $D = \mathrm{diag}(d_1, d_2)$ the diagonal matrix with entries d_1, d_2, so

$$\det(M - \lambda I) = \lambda^2 + \alpha_1(k)\lambda + \alpha_0(k) = 0 \tag{A.2}$$

where

$$\begin{aligned} \alpha_0(k) = & \quad \det(M) = d_1 d_2 k^4 - (d_1 a_{22} + d_2 a_{11})k^2 + \det(A), \\ \alpha_1(k) = & \quad -\mathrm{tr}(M) = (d_1 + d_2)k^2 - \mathrm{tr}(A) > 0. \end{aligned}$$

Splitting (A.2) in real and imaginary parts:

$$\begin{aligned} &\mathrm{Re}(\lambda)^2 - \mathrm{Im}(\lambda)^2 + \alpha_1(k)\,\mathrm{Re}(\lambda) + \alpha_0(k) = 0 \\ &2\,\mathrm{Re}(\lambda)\,\mathrm{Im}(\lambda) + \alpha_1(k)\,\mathrm{Im}(\lambda) = 0 \end{aligned}$$

and looking for critical spectrum, $\mathrm{Re}(\lambda) = 0$, from the second equation it follows that $\mathrm{Im}(\lambda) = 0$ and substituting this in the former yields $\alpha_0(k) = 0$. Since $\mathrm{Im}(\lambda) = 0$, Turing–Hopf instability is impossible. Traveling solutions away-from-equilibrium can still exist though, confer e.g the FitzHugh–Nagumo PDE [64].

The equation $\alpha_0(k) = 0$ shows that the Turing instability can only occur if $d_1 a_{22} + d_2 a_{11} > 0$, meaning that (since $\mathrm{tr}(A(\bar{u}, \bar{v})) < 0$) either $a_{11} > 0$ or $a_{22} > 0$. Without loss of generality we may assume that $a_{22} > 0$. From $\det(A(\bar{u}, \bar{v})) > 0$ it now follows that either $a_{12} > 0$ or $a_{21} > 0$. The two corresponding systems are depicted in Fig. A.8, with the first component now denoted by O (if $a_{12} < 0$ and $a_{21} > 0$) or $P - O$ (if $a_{21} > 0$ and $a_{12} < 0$) and the second component by B. Since the two systems can be transformed into each other by replacing O by $P - O$, with P a sufficiently large constant to retain positivity, in some sense there is only one two-component Turing system.

Remark. There is some disagreement on the definition of activator in the literature. All authors would agree that in the right panel of Fig. A.8, B is the activator. In the left panel, most authors still identify B as the activator whereas in the definition of [59], O is now the activator. To avoid confusion, in this article B will be described as self-activating.

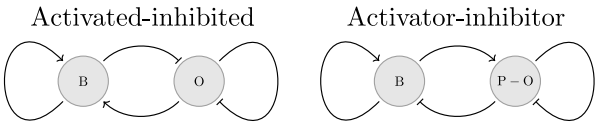

Fig. A.8. Two-component reaction–diffusion systems in equilibrium that admit a Turing instability: activated–inhibited vs activator–inhibitor. Left: component B is activated ($\rightarrow$) by itself and by O; component O is inhibited ($\dashv$) by itself and component B. Component O is sometimes referred to as depleted substance [57] or substrate [58]. Right: by replacing O by $P - O$, with P a constant such that positivity is retained, the inhibition of O by B is replaced by an activation of $P - O$ by B, and the opposite holds for the activation of B by O. Now B activates itself and $P - O$; $P - O$ inhibits itself and B.

A.2. Routh–Hurwitz criterion of three-component Turing(-Hopf) systems

The Routh–Hurwitz criterion provides necessary and sufficient conditions on linear stability of a linear system of equations. For self-containment, a derivation in the special case of three-component (Turing) systems is given. The dispersion relation (8),

$$\det(M - \lambda I) = -\lambda^3 + \beta_2(k)\lambda^2 + \beta_1(k)\lambda + \beta_0(k) = 0$$

can be split into real and imaginary parts

$$\begin{aligned}
&- \operatorname{Re}(\lambda)^3 + 3\operatorname{Re}(\lambda)\operatorname{Im}(\lambda)^2 + \beta_2(k)\operatorname{Re}(\lambda)^2 - \beta_2(k)\operatorname{Im}(\lambda)^2 \\
&\quad + \beta_1(k)\operatorname{Re}(\lambda) + \beta_0(k) = 0 \\
&- 3\operatorname{Re}(\lambda)^2\operatorname{Im}(\lambda) + \operatorname{Im}(\lambda)^3 + 2\beta_2(k)\operatorname{Re}(\lambda)\operatorname{Im}(\lambda) + \beta_1(k)\operatorname{Im}(\lambda) \\
&\quad = 0
\end{aligned}$$

and assuming criticality ($\operatorname{Re}(\lambda) = 0$) gives

$$\begin{aligned}
&-\beta_2(k)\operatorname{Im}(\lambda)^2 + \beta_0(k) = 0 \\
&\operatorname{Im}(\lambda)^3 + \beta_1(k)\operatorname{Im}(\lambda) = 0
\end{aligned}$$

so that we have marginal Turing instability ($\operatorname{Im}(\lambda) = 0$ and $\beta_0(k) = 0$) or marginal Turing–Hopf instability ($\operatorname{Im}(\lambda) = \pm\sqrt{\frac{\beta_0(k)}{\beta_2(k)}} = \pm\sqrt{-\beta_1(k)}$, so $\beta_0(k) + \beta_1(k)\beta_2(k) = 0$ with $\beta_0(k), \beta_1(k) < 0$).

Appendix B. Simplification of the Gilad model

Here we compute that (23) holds.

$$\begin{aligned}
G_B(\mathbf{x}) =& jr_1 \int_{\mathbb{R}^2} G(\mathbf{x},\mathbf{y})W(\mathbf{y})d\mathbf{y} \\
=& jr_1 \int_{\mathbb{R}^2} \frac{1}{2\pi S_0^2} \exp\left(-\frac{|\mathbf{x}-\mathbf{y}|^2}{2\left(S_0(1+\eta B(\mathbf{x}))\right)^2}\right) W(\mathbf{y})d\mathbf{y} \\
=& jr_1(1+\eta B(\mathbf{x}))^2 \int_{\mathbb{R}^2} \frac{1}{2\pi S_0^2} \exp\left(-\frac{|\mathbf{y}'|^2}{2S_0^2}\right) \\
&\times W\left(\frac{\mathbf{y}'}{1+\eta B(\mathbf{x})} + \mathbf{x}\right) d\mathbf{y}' \\
\to& jr_1(1+\eta B(\mathbf{x}))^2 \left(\delta(\mathbf{y}') * W\left(\frac{\mathbf{y}'}{1+\eta B(\mathbf{x})} + \mathbf{x}\right)\right) \\
=& jr_1(1+\eta B(\mathbf{x}))^2 W(\mathbf{x})
\end{aligned}$$

as $S_0 \to 0$ where we used the substitution $\mathbf{y} = \frac{\mathbf{y}'}{1+\eta B(\mathbf{x})} + \mathbf{x}$ (and δ is the Dirac distribution). For the other integral, we follow the same procedure and in addition use the mean value theorem:

$$\begin{aligned}
G_W(\mathbf{x}) =& r_1 \int_{\mathbb{R}^2} G(\mathbf{y},\mathbf{x},t)B(\mathbf{y})d\mathbf{y} \\
=& r_1 \int_{\mathbb{R}^2} \frac{1}{2\pi S_0^2} \exp\left(-\frac{|\mathbf{y}-\mathbf{x}|^2}{2\left(S_0(1+\eta B(\mathbf{y}))\right)^2}\right) B(\mathbf{y})d\mathbf{y} \\
=& r_1 \int_{\mathbb{R}^2} \frac{1}{2\pi S_0^2} \exp\left(-\frac{|\mathbf{y}-\mathbf{x}|^2}{2\left(S_0(1+\eta B(\mathbf{x}))\right)^2}\right) B(\mathbf{y})d\mathbf{y} \\
&+ r_1 \int_{\mathbb{R}^2} \frac{1}{2\pi S_0^2} \exp\left(-\frac{|\mathbf{y}-\mathbf{x}|^2}{2\left(S_0(1+\eta B(\mathbf{z}))\right)^2}\right) \\
&\times \frac{\eta|\mathbf{y}-\mathbf{x}|^2\nabla_{\mathbf{y}}B(\mathbf{z})\cdot(\mathbf{y}-\mathbf{x})}{S_0^2(1+\eta B(\mathbf{z}))} B(\mathbf{y})d\mathbf{y} \\
\to& jr_1(1+\eta B(\mathbf{x}))^2 \left(\delta(\mathbf{y}') * B\left(\frac{\mathbf{y}'}{1+\eta B(\mathbf{x})} + \mathbf{x}\right)\right) \\
&+ jr_1(1+\eta B(\mathbf{z}))^4 \left(\delta(\mathbf{y}') * \left(\frac{\eta|\mathbf{y}'|^2\nabla_{\mathbf{y}}B(\mathbf{z})\cdot\mathbf{y}'}{S_0^2}\right.\right. \\
&\left.\left.\times B\left(\frac{\mathbf{y}'}{1+\eta B(\mathbf{z})} + \mathbf{x}\right)\right)\right) \\
=& jr_1(1+\eta B(\mathbf{x}))^2 B(\mathbf{x}).
\end{aligned}$$

References

[1] W. Macfadyen, Vegetation patterns in the semi-desert plains of british somaliland, Geogr. J. 116 (1950) 199–211.
[2] V. Deblauwe, N. Barbier, P. Couteron, O. Lejeune, J. Bogaert, The global biogeography of semi-arid periodic vegetation patterns, Global Ecol. Biogeogr. 17 (2008) 715–723.
[3] M. Rietkerk, S.C. Dekker, P.C. de Ruiter, J. van de Koppel, Self-organized patchiness and catastrophic shifts in ecosystems, Science 305 (2004) 1926–1929.
[4] M. Scheffer, J. Bascompte, W.A. Brock, V. Brovkin, S.R. Carpenter, V. Dakos, H. Held, E.H. van Nes, M. Rietkerk, G. Sugihara, Early-warning signals for critical transitions, Nature 461 (2009) 53–59.
[5] S. Kéfi, V. Guttal, W.A. Brock, S.R. Carpenter, A.M. Ellison, V.N. Livina, D.A. Seekell, M. Scheffer, E.H. van Nes, V. Dakos, Early warning signals of ecological transitions: Methods for spatial patterns, PLOS ONE 9 (3) (2014) 1–13.
[6] C.A. Klausmeier, Regular and irregular patterns in semi-arid vegetation, Science 284 (1999) 1826–1828.
[7] S.E. Thompson, C.J. Harman, P. Heine, G.G. Katul, Vegetation-infiltration relationships across climatic and soil type gradients, J. Geophys. Res.: Biogeosci. 115 (2010).
[8] D.J. Tongway, C. Valentin, J. Seghieri, Banded Vegetation Patterning in Arid and Semiarid Environments, Springer-Verlag, New York, New York, USA, 2001.
[9] M. Rietkerk, P. Ketner, J. Burger, B. Hoorens, H. Olff, Multiscale soil and vegetation patchiness along a gradient of herbivore impact in a semi-arid grazing system in west africa, Plant Ecol. 148 (2000) 207–224.
[10] M. Rietkerk, J. van de Koppel, Regular pattern formation in real ecosystems, Trends Ecol. Evol. 23 (2008) 169–175.
[11] R. HilleRisLambers, M. Rietkerk, F.V.D. Bosch, H.H.T. Prins, H.D. Kroon, Vegetation pattern formation in semi-arid grazing systems, Ecology 82 (2001) 50–61.
[12] E. Gilad, J. von Hardenberg, A. Provenzale, M. Shachak, E. Meron, Ecosystem engineers: From pattern formation to habitat creation, Phys. Rev. Lett. 93 (2004) 1–4.
[13] A. Turing, The chemical basis of morphogenesis, Phil. Trans. R. Soc. B 237 (1952) 37–72.
[14] K. Siteur, E. Siero, M.B. Eppinga, J.D.M. Rademacher, A. Doelman, M. Rietkerk, Beyond Turing: the response of patterned ecosystems to environmental change, Ecol. Complex. 20 (2014) 81–96.
[15] E. Siero, A. Doelman, M.B. Eppinga, J.D.M. Rademacher, M. Rietkerk, K. Siteur, Striped pattern selection by advective reaction-diffusion systems: Resilience of banded vegetation on slopes, Chaos 25 (2015).
[16] A.S. Dagbovie, J.A. Sherratt, Pattern selection and hysteresis in the rietkerk model for banded vegetation in semi-arid environments, J. R. Soc. Interface 11 (99) (2014) 20140465.
[17] J. von Hardenberg, E. Meron, M. Shachak, Y. Zarmi, Diversity of vegetation patterns and desertification, Phys. Rev. Lett. 87 (2001) 3–6.
[18] Y.R. Zelnik, S. Kinast, H. Yizhaq, G. Bel, E. Meron, Regime shifts in models of dryland vegetation, Phil. Trans. R. Soc. A 371 (2013).
[19] M. Rietkerk, M.C. Boerlijst, F. van Langevelde, R. Hillerislambers, J. van de Koppel, L. Kumar, H.H.T. Prins, A.M. de Roos, Self-organization of vegetation in arid ecosystems, Amer. Nat. 160 (2002) 524–530.
[20] Y.R. Zelnik, E. Meron, G. Bel, Gradual regime shifts in fairy circles, Proc. Natl. Acad. Sci. 112 (40) (2015) 12327–12331.
[21] E. Meron, Pattern formation – a missing link in the study of ecosystem response to environmental changes, Math. Biosci. 271 (2016) 1–18.

[22] H. Uecker, D. Wetzel, J.D.M. Rademacher, Pde2path - A Matlab package for continuation and bifurcation in 2D elliptic systems, Numer. Math. Theory Methods Appl. 7 (2014) 58–106.
[23] H. Uecker, Pattern formation with pde2path, 2020, arXiv:1908.05211.
[24] E. Gilad, J. von Hardenberg, A. Provenzale, M. Shachak, E. Meron, A mathematical model of plants as ecosystem engineers, J. Theoret. Biol. 244 (4) (2007) 680–691.
[25] K. Gowda, Y. Chen, S. Iams, M. Silber, Assessing the robustness of spatial pattern sequences in a dryland vegetation model, Proc. R. Soc. A 472 (2187) (2016).
[26] J.A. Sherratt, History-dependent patterns of whole ecosystems, Ecol. Complex. 14 (2013) 8–20.
[27] E. Siero, Nonlocal grazing in patterned ecosystems, J. Theoret. Biol. 436 (2018) 64–71.
[28] E. Siero, K. Siteur, A. Doelman, J. van de Koppel, M. Rietkerk, M.B. Eppinga, Grazing away the resilience of patterned ecosystems, Amer. Nat. (2019).
[29] P. Gray, S.K. Scott, Autocatalytic reactions in the isothermal, continuous stirred tank reactor: oscillations and instabilities in the system a + 2b → 3b, b → c, Chem. Eng. Sci. 39 (1984) 1087–1097.
[30] J.E. Pearson, Complex patterns in a simple system, Science 261 (1993) 189–192.
[31] S. van der Stelt, A. Doelman, G. Hek, J.D.M. Rademacher, Rise and fall of periodic patterns for a Generalized Klausmeier-Gray-Scott model, J. Nonlinear Sci. 23 (2013) 39–95.
[32] E. Meron, Nonlinear Physics of Ecosystems, CRC Press, 2015.
[33] P. Gandhi, S. Bonetti, S. Iams, A. Porporato, M. Silber, A fast–slow model of banded vegetation pattern formation in drylands, Physica D 410 (2020) 132534.
[34] S. Kéfi, M.B. Eppinga, P.C. de Ruiter, M. Rietkerk, Bistability and regular spatial patterns in arid ecosystems, Theor. Ecol. 3 (4) (2010) 257–269.
[35] H. Meinhardt, Turing's theory of morphogenesis of 1952 and the subsequent discovery of the crucial role of local self-enhancement and long-range inhibition, Interface Focus 2 (4) (2012) 407–416.
[36] A. Nakamasu, G. Takahashi, A. Kanbe, S. Kondo, Interactions between zebrafish pigment cells responsible for the generation of turing patterns, Proc. Natl. Acad. Sci. 106 (21) (2009) 8429–8434.
[37] S. Getzin, H. Yizhaq, B. Bell, T.E. Erickson, A.C. Postle, I. Katra, O. Tzuk, Y.R. Zelnik, K. Wiegand, T. Wiegand, E. Meron, Discovery of fairy circles in Australia supports self-organization theory, Proc. Natl. Acad. Sci. 113 (13) (2016) 3551–3556.
[38] C. Fernandez-Oto, D. Escaff, J. Cisternas, Spiral vegetation patterns in high-altitude wetlands, Ecol. Complex. 37 (2019) 38–46.
[39] M. Tlidi, M.G. Clerc, D. Escaff, P. Couteron, M. Messaoudi, M. Khaffou, A. Makhoute, Observation and modelling of vegetation spirals and arcs in isotropic environmental conditions: dissipative structures in arid landscapes, Phil. Trans. R. Soc. A 376 (2135) (2018) 20180026.
[40] L. Larsen, C. Thomas, M. Eppinga, T. Coulthard, Exploratory modeling: Extracting causality from complexity, EOS Trans. Am. Geophys. Union 95 (32) (2014) 285–286.
[41] A.Y. Kletter, J. von Hardenberg, E. Meron, A. Provenzale, Patterned vegetation and rainfall intermittency, J. Theoret. Biol. 256 (4) (2009) 574–583.
[42] K. Siteur, M.B. Eppinga, D. Karssenberg, M. Baudena, M.F.P. Bierkens, M. Rietkerk, How will increases in rainfall intensity affect semiarid ecosystems?, Water Resour. Res. 50 (7) (2014) 5980–6001.
[43] O. Crompton, A. Sytsma, S. Thompson, Emulation of the saint venant equations enables rapid and accurate predictions of infiltration and overland flow velocity on spatially heterogeneous surfaces, Water Resour. Res. 55 (8) (2019) 7108–7129.
[44] L. Eigentler, J.A. Sherratt, Effects of precipitation intermittency on vegetation patterns in semi-arid landscapes, Physica D 405 (2020) 132396.
[45] P. Barbosa, J. Hines, I. Kaplan, H. Martinson, A. Szczepaniec, Z. Szendrei, Associational resistance and associational susceptibility: Having right or wrong neighbors, Annu. Rev. Ecol. Evol. Syst. 40 (2009) 1–20.
[46] K. Gowda, H. Riecke, M. Silber, Transitions between patterned states in vegetation models for semiarid ecosystems, Phys. Rev. E 89 (2014).
[47] M.W. van Rooyen, G.K. Theron, N. van Rooyen, W.J. Jankowitz, W.S. Matthews, Mysterious circles in the namib desert: review of hypotheses on their origin, J. Arid Environ. 57 (4) (2004) 467–485.
[48] W.R. Tschinkel, Experiments testing the causes of namibian fairy circles, PLoS One 10 (10) (2015).
[49] V. Deblauwe, P. Couteron, O. Lejeune, J. Bogaert, N. Barbier, Environmental modulation of self-organized periodic vegetation patterns in sudan, Ecography 34 (2011) 990–1001.
[50] V. Deblauwe, P. Couteron, J. Bogaert, N. Barbier, Determinants and dynamics of banded vegetation pattern migration in arid climates, Ecol. Monograph 82 (2012) 3–21.
[51] N. Barbier, P. Couteron, V. Deblauwe, Case study of self-organized vegetation patterning in dryland regions of Central Africa, in: Patterns of Land Degradation in Drylands: Understanding Self-Organised Ecogeomorphic Systems, Springer, 2014.
[52] J.A. Sherratt, Using wavelength and slope to infer the historical origin of semiarid vegetation bands, Proc. Natl. Acad. Sci. 112 (14) (2015) 4202–4207.
[53] R. Bastiaansen, O. Jaïbi, V. Deblauwe, M.B. Eppinga, K. Siteur, E. Siero, S. Mermoz, A. Bouvet, A. Doelman, M. Rietkerk, Multistability of model and real dryland ecosystems through spatial self-organization, Proc. Natl. Acad. Sci. 115 (44) (2018) 11256–11261.
[54] K. Gowda, S. Iams, M. Silber, Signatures of human impact on self-organized vegetation in the horn of africa, Sci. Rep. 8 (1) (2018).
[55] P. Gandhi, L. Werner, S. Iams, K. Gowda, M. Silber, A topographic mechanism for arcing of dryland vegetation bands, J. R. Soc. Interface 15 (147) (2018).
[56] L.A. Segel, J.L. Jackson, Dissipative structure: An explanation and an ecological example, J. Theoret. Biol. 37 (3) (1972) 545–559.
[57] A. Gierer, H. Meinhardt, A theory of biological pattern formation, Kybernetik 12 (1972) 30–39.
[58] L. Edelstein-Keshet, Mathematical Models in Biology, Society for Industrial and Applied Mathematics, 2005.
[59] J.D. Murray, Mathematical Biology II: Spatial Models and Biomedical Applications, Springer New York, 2003.
[60] A. Anma, K. Sakamoto, T. Yoneda, Unstable subsystems cause Turing instability, Kodai Math. J. 35 (2) (2012) 215–247.
[61] S. Hata, H. Nakao, A.S. Mikhailov, Sufficient conditions for wave instability in three-component reaction-diffusion systems, Prog. Theor. Exp. Phys. (2014).
[62] R.A. Satnoianu, M. Menzinger, P.K. Maini, Turing instabilities in general systems, J. Math. Biol. 41 (6) (2000) 493–512.
[63] K.A.J. White, C.A. Gilligan, Spatial heterogeneity in three species, plant-parasite-hyperparasite, systems, Phil. Trans. R. Soc. Lond. B 353 (1368) (1998) 543–557.
[64] J. Nagumo, S. Arimoto, S. Yoshizawa, An active pulse transmission line simulating nerve axon, Proc. IRE 50 (1962).